



Near-Earth Sub-Alfvénic Solar Winds: Interplanetary Origins and Geomagnetic Impacts

Rajkumar Hajra¹ and Bruce T. Tsurutani²¹ Indian Institute of Technology Indore, Simrol, Indore 453552, India; rajkumarhajra@yahoo.co.in² Jet Propulsion Laboratory, California Institute of Technology, Pasadena, CA 91109, USA

Received 2021 September 14; revised 2021 November 24; accepted 2021 December 11; published 2022 February 18

Abstract

The near-Earth solar wind is in general super-Alfvénic and supermagnetosonic. Using all available near-Earth solar wind measurements between 1973 and 2020, we identified 30 intervals with sub-Alfvénic solar winds. The majority (83%) of the events occurred within interplanetary coronal mass ejection magnetic clouds (MCs)/driver gases. These MC sub-Alfvénic events are characterized by exceptionally low plasma densities (N_{sw}) of ~ 0.04 – 1.20 cm^{-3} , low temperatures (T_{sw}) of $\sim 0.08 \times 10^5 \text{ K}$ to $12.46 \times 10^5 \text{ K}$, enhanced magnetic field intensities (B_0) of ~ 8.3 – 53.9 nT , and speeds (V_{sw}) of ~ 328 – 949 km s^{-1} . The resultant high Alfvén wave speeds (V_A) ranged from ~ 410 to 1471 km s^{-1} . This is consistent with a mechanism of the MC expansions as they propagate radially outward, causing small pockets of sub-Alfvénic wind regions within the MCs. The remainder of the sub-Alfvénic intervals (17%) occurred within the extreme trailing portions of solar wind high-speed streams (HSSs). These HSS sub-Alfvénic winds had low N_{sw} of ~ 0.04 – 0.97 cm^{-3} , low T_{sw} of $\sim 0.06 \times 10^5 \text{ K}$ to $0.46 \times 10^5 \text{ K}$, B_0 of ~ 6.3 – 18.2 nT , V_{sw} of ~ 234 – 388 km s^{-1} , and a V_A range of ~ 364 – 626 km s^{-1} . This is consistent with a mechanism of solar wind super-radial expansions in the trailing HSS regions. During sub-Alfvénic solar wind intervals, Earth’s bow shock nose exhibited rapid evanescence, and the estimated geocentric magnetopause distance increased by $\sim 33\%$ – 86% . The inner magnetosphere was more or less unaffected by the sub-Alfvénic solar winds. No significant impact was observed in the outer radiation belt relativistic electrons, and no geomagnetic storms or substorms were triggered during the sub-Alfvénic solar wind events.

Unified Astronomy Thesaurus concepts: Solar wind (1534); Planetary magnetospheres (997); Solar coronal mass ejections (310); Interplanetary magnetic fields (824); Fast solar wind (1872); Van Allen radiation belts (1758)

1. Introduction

Earth has a strong intrinsic magnetic field ($\sim 3 \times 10^4 \text{ nT}$ at the equatorial surface) that acts as an obstacle to the super-Alfvénic and supermagnetosonic solar wind plasma flow of ~ 400 – 700 km s^{-1} with an average density of $\sim 7 \text{ cm}^{-3}$ and magnetic field of $\sim 6 \text{ nT}$ (Tsurutani et al. 2018). This interaction results in a well-defined dayside bow shock located at ~ 11 – 15 Earth radii (R_\oplus ; $1 R_\oplus \sim 6371 \text{ km}$) upstream of Earth (Fairfield 1971). Earthward of the bow shock is the magnetosheath, where the solar wind is decelerated, compressed, and heated. The boundary layer separating the magnetosheath from the proper magnetosphere is known as the magnetopause (Chapman & Ferraro 1931). While the geomagnetic field lines are compressed on the dayside magnetosphere located around 9 – $10 R_\oplus$ (Fairfield 1971), they are elongated on the nightside, forming the two-lobe magnetotail that extends to a few hundred R_\oplus and beyond (Tsurutani et al. 1984).

The bow shock may disappear during the submagnetosonic solar wind interaction with the magnetosphere. From a survey of the solar wind data time-shifted to Earth’s bow shock, Usmanov et al. (2005) identified 11 cases of sub-Alfvénic/submagnetosonic solar wind intervals between 1963 and 2003. To our knowledge, only five case studies of submagnetosonic/sub-Alfvénic intervals upstream of Earth have been reported to date—on 1979 November 22 (Gosling et al. 1982), 1999 April 26 (Zhou et al. 2000; Fairfield et al. 2001), 1999 May 11

(Usmanov et al. 2000, 2005; Fairfield et al. 2001; Smith et al. 2001), 2002 May 24 (Chané et al. 2012, 2015), and 2013 January 17 (Lugaz et al. 2016). Using an inverse magneto-hydrodynamic mapping method, Usmanov et al. (2000) suggested that the rarefaction of the submagnetosonic/sub-Alfvénic solar wind can be caused by a coronal outflow suppression due to a sudden change in the magnetic field of the Sun during a polar magnetic field reversal. Smith et al. (2001) reported suppression of the magnetic field fluctuations in sub-Alfvénic solar winds. Chané et al. (2012) reported no significant geomagnetic impact of sub-Alfvénic solar winds. Lugaz et al. (2016) reported a rapid and intense loss of electrons in the outer radiation belt during such a solar wind event.

After more than half a century of near-Earth solar wind monitoring, there has been no systematic study on the magnetosphere coupling with the sub-Alfvénic solar winds. Questions remain concerning the solar and interplanetary causes leading to or associated with the sub-Alfvénic winds and their impacts on the magnetosphere of Earth. The aims of the present work are to (1) identify and study sub-Alfvénic solar wind intervals using all near-Earth solar wind measurements available, (2) identify their interplanetary features and/or causes, and (3) determine their geomagnetic impacts, if any. Such a study has never been reported before. This study will hopefully augment our understanding of unique and somewhat rare solar wind–magnetosphere coupling events at Earth, under conditions that are expected to occur more frequently at extrasolar planets (Shkolnik et al. 2005; Saur et al. 2013; Cohen et al. 2014), and which have been reported for the satellites of Jupiter (Io, Europa, and Ganymede) and Saturn



Original content from this work may be used under the terms of the [Creative Commons Attribution 4.0 licence](https://creativecommons.org/licenses/by/4.0/). Any further distribution of this work must maintain attribution to the author(s) and the title of the work, journal citation and DOI.

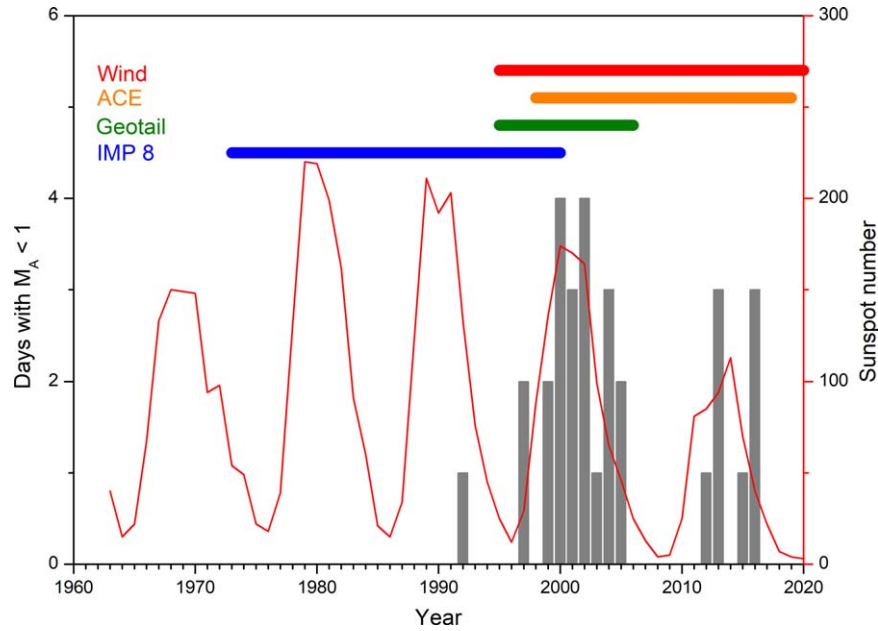


Figure 1. Statistical survey for sub-Alfvénic solar winds with Alfvén Mach number $M_A < 1$. Sunspot numbers (red, legend on the right) indicate the solar activity cycle, starting from the solar minimum with the lowest number, the ascending phase with increasing number, and the maximum value during solar maximum and followed by decreasing number during the descending phase of the solar cycle. Horizontal lines indicate the periods covered by the IMP 8 (blue), Geotail (green), ACE (orange), and Wind (red) spacecraft. The yearly number of intervals with $M_A < 1$ is shown by the gray histogram (the legend is on the left).

(Rhea and Enceladus) (Kivelson et al. 1997; Clarke et al. 2002; Grodent et al. 2006; Kriegel et al. 2011; Mura et al. 2018).

2. Material and Methods

2.1. Survey of Sub-Alfvénic Solar Winds

In order to identify intervals of sub-Alfvénic solar winds, a detailed survey has been made on high-resolution (few seconds to ~ 1 minute) solar wind data upstream of Earth, measured by the spacecraft Interplanetary Monitoring Platform 8 (IMP 8; https://spdf.gsfc.nasa.gov/pub/data/imp/imp8/mag/15s_ascii_v3/) from 1973 November 4 to 2000 June 9, by Geotail (<https://cdaweb.gsfc.nasa.gov/cgi-bin/eval1.cgi>) from 1995 March 15 to 2006 November 17, by Advanced Composition Explorer (ACE; <http://www.srl.caltech.edu/ACE/ASC/>) from 1998 February 5 to 2019 October 10, and by Wind (<https://spdf.gsfc.nasa.gov/pub/data/wind/>) from 1995 January 1 to 2020 December 31. The spacecraft measurements are shifted by the solar wind transit time to the arrival at Earth’s bow shock nose. The data coverage interval of each spacecraft is shown by color-coded horizontal lines in Figure 1. The time period (1973–2020) covers more than four solar cycles, as shown by variation of the yearly mean smoothed sunspot numbers (SSNs) obtained from the Royal Observatory of Belgium, Brussels (<http://www.sidc.be/silso/home>).

We have used the interplanetary magnetic field (IMF) data measured in geocentric solar ecliptic (GSE) coordinates, where the x -axis is directed from Earth toward the Sun and the y -axis is in the ecliptic plane (the plane of Earth’s orbit around the Sun) pointing toward dusk. The z -axis is perpendicular to the ecliptic plane (positive north). Using the solar wind plasma and IMF measurements, we estimated the local magnetosonic speed as $V_{ms} = \sqrt{V_A^2 + V_S^2}$, where V_A is the Alfvén speed ($B_0/\sqrt{\mu_0\rho}$), V_S is the sound speed ($\sqrt{5k_B(T_p + T_e)/3m_p}$), B_0 is the IMF magnitude, μ_0 is the free space permeability, ρ

denotes the solar wind mass density, k_B is the Boltzmann constant, T_p and T_e are the proton and electron temperatures, respectively, and m_p is the proton mass. The magnetosonic and Alfvén Mach numbers are defined as $M_{ms} = V_{sw}/V_{ms}$ and $M_A = V_{sw}/V_A$, respectively. From the above expressions, $M_{ms} < M_A$.

Thirty intervals have been found with $M_A < 1$ from 1973 to 2020. Table 1 lists the minimum M_A value, corresponding date and time, associated interplanetary structure (to be defined later), and the spacecraft encountering each of the intervals. Owing to the highly varying nature of the solar wind, M_A may not be continuously < 1 in some cases. However, if an $M_A < 1$ event is followed by $M_A > 1$ for more than 30 minutes, we have considered this to be the end of the sub-Alfvénic interval. It should be noted that this statistic is based on only solar wind measurements with ~ 1 minute or higher resolution (we did not include the intervals when only lower-resolution data are available). Second, we did not consider cases when there are data gaps at the beginning and/or at the end of a sub-Alfvénic interval. It can be noted in Figure 1 that no sub-Alfvénic intervals were recorded in our study from 1973 through 1991. The lack of events seems to be related to the lack of sufficient satellite coverage during 1973–1991, the data quality of IMP 8, or both.

The present survey indicates that Earth may encounter one sub-Alfvénic solar wind event every 2 yr. Most interestingly, 20 of the sub-Alfvénic intervals occurred during solar cycle 23 (1996–2008). This result indicates a high probability of Earth being encountered by a sub-Alfvénic solar wind, in contrast to the reported rate of two or three events per decade (Usmanov et al. 2005). This result may be due to the recent low solar activity during solar cycle 23. We are currently examining this possibility. However, this is beyond the scope of the present paper.

Table 1
The Sub-Alfvénic Solar Winds under This Study

S. No.	M_A Minimum	Date	Time	Interplanetary Structure ^a	Detecting Spacecraft
1	0.38	1992 Nov 9	19:15	MC	IMP 8
2	0.90	1997 Apr 11	11:22	MC	Geotail
3	0.82	1997 Nov 22	19:18	MC	Wind
4	0.80	1999 Apr 27	04:17	HSS tail	Wind, ACE
5	0.60	1999 May 11	18:36	HSS tail	Wind, ACE
6	0.61	2000 Mar 29	06:37	MC	Wind
7	0.67	2000 Jul 16	01:49	MC	Geotail, ACE
8	0.75	2000 Jul 16	04:49	MC	Geotail, ACE
9	0.66	2000 Aug 12	12:33	MC	Geotail
10	0.98	2001 Apr 12	08:26	MC	ACE
11	0.90	2001 Jun 19	13:11	MC	Wind, ACE
12	0.79	2001 Nov 24	22:29	MC	Wind, ACE
13	0.54	2002 Mar 20	10:35	MC	Wind, ACE
14	0.48	2002 May 24	23:43	MC	Wind, ACE
15	0.43	2002 May 25	10:39	MC	Wind, ACE
16	0.60	2002 Jul 19	17:08	MC	ACE
17	0.84	2003 Oct 2	07:10	HSS tail	Wind
18	0.85	2004 Jul 23	03:43	MC	Wind, ACE
19	0.70	2004 Sep 12	06:52	HSS tail	Wind
20	0.45	2004 Sep 13	01:52	HSS tail	Wind
21	0.80	2005 May 15	09:44	MC	Wind, ACE
22	0.90	2005 May 15	23:02	MC	Wind, ACE
23	0.90	2012 Jul 16	05:16	MC	Wind
24	0.60	2013 Jan 17	20:12	MC	Wind, ACE
25	0.70	2013 Jan 17	23:20	MC	Wind, ACE
26	0.88	2013 Oct 3	03:13	MC	Wind
27	0.70	2015 Jun 23	10:48	MC	Wind, ACE
28	0.82	2016 Oct 13	12:22	MC	Wind, ACE
29	0.81	2016 Oct 13	23:07	MC	Wind, ACE
30	0.71	2016 Oct 14	02:56	MC	Wind, ACE

Note.

^a To be defined later.

2.2. Solar and Interplanetary Events

To identify the solar sources of the sub-Alfvénic winds, various solar data are explored. The coronal mass ejection (CME) information is obtained from the CME catalog available at the Coordinated Data Analysis Workshops (CDAW; https://cdaw.gsfc.nasa.gov/CME_list/index.html). The catalog is based on the observations made by the Large Angle and Spectrometric Coronagraph (LASCO) on board the Solar and Heliospheric Observatory (SOHO). Near the Sun, a CME has three parts: a bright loop at the outer antisolar extent, a dark region in the middle, and a bright, high-density filament near the base (e.g., Illing & Hundhausen 1986). When a CME erupts from the Sun and propagates through the interplanetary medium, it is possible that the parts may evolve and that not all three parts may reach 1 au together. Thus, the interplanetary counterpart of a CME is called an interplanetary CME (ICME).

A fast ICME propagating (with a speed $V_{sw} > 500 \text{ km s}^{-1}$) faster than the local upstream V_{ms} (typically $\sim 70\text{--}100 \text{ km s}^{-1}$) in the plasma frame can generate an upstream fast forward (FF) shock, followed by an interplanetary sheath of compressed, heated, and turbulent solar wind plasma and large-amplitude IMF variations (e.g., Kennel et al. 1985; Tsurutani et al. 1988). As a result, the plasma temperature T_{sw} , density N_{sw} , and IMF magnitude B_0 increase in the sheath downstream of the FF shock.

To determine whether an interplanetary discontinuity with the abrupt increases in V_{sw} , N_{sw} , T_{sw} , and B_0 is a shock or not,

we performed “shock analysis” on the plasma and magnetic field data (e.g., Smith 1985, p. 69; Tsurutani & Lin 1985; Tsurutani et al. 2011c; Hajra et al. 2016, 2020; Hajra & Tsurutani 2018a; Hajra 2021). The plasma flow and magnetic field mixed-mode technique (Abraham-Shrauner & Yun 1976) and the Rankine–Hugoniot conservation equations (Rankine 1870; Hugoniot 1887, 1889) are used to determine the discontinuity normal vector, propagation angle (θ_{Bn}) with respect to the upstream IMF, and discontinuity magnetosonic Mach number M_{ms} . Discontinuities with $M_{ms} > 1$ are FF shocks.

Only a few of the ICMEs, known as flux rope magnetic clouds (MCs), are characterized by a smooth and slow rotation in the IMF component(s) as defined by Burlaga et al. (1981) and Klein & Burlaga (1982). We have used a discriminator of a high IMF B_0 , a reduced T_{sw} , and a low plasma β (β is defined as the ratio of the plasma thermal pressure to the magnetic pressure) as the identifier of an MC/“driver gas” (Tsurutani & Gonzalez 1997, pp. 77–89). In examining these MC/driver gas events, we were unable to find any unifying magnetic features that could identify any non–flux rope events.

Another important space weather event is the solar wind high-speed stream (HSS; Krieger et al. 1973; Sheeley et al. 1976) emanated from a coronal hole. An HSS is identified by eye inspection of the solar wind speed V_{sw} temporal profile using the criterion $500 \text{ km s}^{-1} < V_{sw} \leq 850 \text{ km s}^{-1}$. Coronal images taken by the Atmospheric Imaging Assembly (AIA)

telescope (Lemen et al. 2012) on board NASA’s Solar Dynamics Observatory (SDO; Pesnell et al. 2012) are explored to verify the solar source of an HSS. An HSS is led by a compressed magnetic field and plasma region called a corotating interaction region (CIR; Smith & Wolfe 1976; Tsurutani et al. 1995). The CIRs are also used to identify HSSs.

2.3. Variance Analysis

Variance analysis is a useful tool to quantify periodic variations or fluctuations in magnetic field data. We used the IMF components to construct the field variances (σ_x^2 , σ_y^2 , σ_z^2) at three time intervals, 5, 15, and 45 minutes, and make 45 minute averages of the variances. A high variance value indicates a large amount of wave power for frequencies up to the variance time value, while a low variance implies reduced wave power in that frequency range (Tsurutani et al. 1982, 2011b; Hajra et al. 2013, 2017). Thus, the combined variances can be considered as a low-resolution power spectrum.

The variances are normalized by the square of the IMF B_0 to obtain the normalized variances (σ_x^2/B_0^2 , σ_y^2/B_0^2 , σ_z^2/B_0^2). For any data interval analyzed, the 45 minute average of the 5 minute variance has a magnitude less than the 45 minute average of the 15 minute variance, and the latter has a magnitude less than the 45 minute variance. In other words, the shorter-interval variances are “nested” inside the longer-interval variances. In this paper we call these the “nested normalized variances.”

2.4. Geomagnetic and Radiation Belt Variations

To study the impact of the solar wind variations on the magnetosphere, we estimated the bow shock (r_{BS}) and magnetopause (r_{MP}) locations by typical models such as Farris & Russell (1994) and Shue et al. (1998). Magnetic storm activity is studied using the symmetric ring current index SYM-H variation (1 minute resolution). The latter are obtained from the World Data Center for Geomagnetism, Kyoto, Japan (WDC; <http://wdc.kugi.kyoto-u.ac.jp/>). During geomagnetic storms (Chapman & Bartels 1940; Gonzalez et al. 1994), enhancement of the westward ring current (Dessler & Parker 1959) is reflected in the decreases in the SYM-H index (Wanliss & Showalter 2006; Iyemori et al. 2010). During auroral substorm activity (Akasofu 1964), the auroral ionospheric (westward) electrojet current is enhanced. The latter has been studied using the SuperMAG AL or the SML index (1 minute resolution), obtained from <https://supermag.jhuapl.edu/> (Gjerloev 2009).

To study the variation of the outer radiation belt, the integrated fluxes (1 minute resolution) of electrons with energies $E > 0.6$ and > 2.0 MeV at geosynchronous orbit ($L = 6.6$) were obtained from the Geostationary Operational Environment Satellites (GOES; <http://www.ngdc.noaa.gov/stp/satellite/goes/dataaccess.html>; Onsager et al. 1996). The McIlwain L -parameter represents the radial distance in the R_\oplus unit at the magnetic equator for a dipole approximation of Earth’s magnetic field (McIlwain 1961). For general time coverage, data for events during 1992–1994 are obtained from GOES-7, those for 1995–2002 from GOES-8, those for 2003–2010 from GOES-12, and those for the 2011–2016 events from GOES-13.

3. Results and Discussion

3.1. Sub-Alfvénic Solar Wind and Geomagnetic Variation on 2002 March 18–21

Figure 2 shows the solar wind plasma and magnetic field measurements and geomagnetic variations during 2002 March 18–21. The solar wind measurements are taken by the Wind spacecraft between ~ 40 and $\sim 60 R_\oplus$ upstream of Earth and shifted to Earth’s bow shock nose in order to compare with their geomagnetic impacts (Figure 2(f), blue). The plasma and magnetic field measurements are taken from the Solar Wind Experiment (Ogilvie et al. 1995) and the Magnetic Field Investigation (Lepping et al. 1995) instruments, respectively, on board Wind.

The solar wind/interplanetary variations show the interplanetary counterpart of a CME or an ICME. The CME was ejected from the Sun at $\sim 02:54$ universal time (UT) on March 18 and had a speed of $\sim 990 \text{ km s}^{-1}$. The arrival of a shock ahead of the ICME is identified by a sharp increase in the solar wind speed V_{sw} (from ~ 300 to $\sim 485 \text{ km s}^{-1}$) at $\sim 13:13$ UT on March 18 (Figure 2(a), black). This is marked by a vertical dashed line in Figure 2. There are simultaneous increases in the plasma density N_{sw} (from ~ 14 to $\sim 53 \text{ cm}^{-3}$), ram pressure P_{sw} (from ~ 2 to $\sim 22 \text{ nPa}$), temperature T_{sw} (from $\sim 0.4 \times 10^5 \text{ K}$ to $\sim 3.7 \times 10^5 \text{ K}$), and the IMF B_0 (from ~ 6 to $\sim 13 \text{ nT}$). The “shock analysis” indicates that the discontinuity is an interplanetary FF shock with an M_{ms} of ~ 3.4 propagating at an angle (θ_{Bn}) of $\sim 39^\circ$ relative to the upstream ambient IMF.

The (ram) pressure increase across the interplanetary shock ahead of the ICME causes an earthward movement of the bow shock and the magnetopause nose (Figure 2(f)). There is a simultaneous and sharp increase in the geomagnetic SYM-H index to $+81 \text{ nT}$ (Figure 2(h), black), which is called a sudden impulse (SI^+). The SML index exhibited an abrupt decrease to -266 nT at the time of the shock impact (Figure 2(h), red). While the > 2.0 MeV electron fluxes remain more or less unchanged, the > 0.6 MeV electrons exhibit decreases in the flux following the shock (Figure 2(g)). The > 0.6 MeV electron flux decrease can be caused by either gradient drift loss to the magnetosheath, called “magnetopause shadowing” (West et al. 1972), or losses to the ionosphere by wave–particle interactions (Tsurutani et al. 2016).

The interplanetary shock (at $\sim 13:13$ UT on March 18) is followed by an interplanetary sheath, characterized by enhancements in the plasma parameters N_{sw} , P_{sw} , and T_{sw} and large fluctuations in the IMF components B_x , B_y , and B_z up to $\sim 06:10$ UT on March 19 (marked by a horizontal green bar on the top, Figure 2). The ~ 3.4 hr southward component of the sheath IMF with a minimum $B_z \sim -15 \text{ nT}$ (Figure 2(e), red) caused a magnetic storm main phase development, as can be observed in the SYM-H decrease (Figure 2(h), black). The storm has a peak SYM-H intensity of -66 nT (moderate-intensity storm; Gonzalez et al. 1994) at $\sim 06:01$ UT on March 19. During the storm main phase, six weak substorms are recorded with the SML peak intensities of -289 nT (at $\sim 17:55$ UT on March 18), -253 nT (at $\sim 19:33$ UT on March 18), -388 nT (at $\sim 00:50$ UT on March 19), -430 nT (at $\sim 01:40$ UT on March 19), -527 nT (at $\sim 04:37$ UT on March 19), and -435 nT (at $\sim 05:27$ UT on March 19) (Figure 2(h), red). A large-scale (~ 3 orders of magnitude) > 0.6 MeV electron flux loss occurs associated with the shock impingement on the magnetosphere followed by the sheath. This observation is

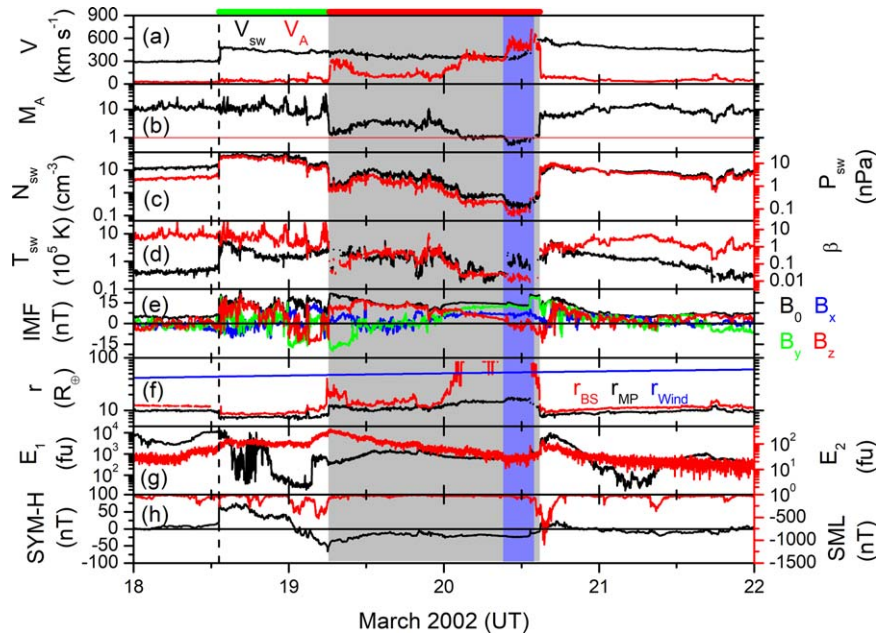


Figure 2. Solar wind variations and geomagnetic effects on 2002 March 18–21. From top to bottom, the panels are (a) the solar wind plasma velocity V_{sw} (black) and Alfvén velocity V_A (red); (b) the Alfvén Mach number M_A ; (c) the solar wind plasma density N_{sw} (black; legend on the left) and ram pressure P_{sw} (red; legend on the right); (d) the plasma temperature T_{sw} (black; legend on the left) and the plasma β (red; legend on the right); (e) the IMF magnitude B_0 (black) and B_x (blue), B_y (green), and B_z (red) components; (f) the calculated geocentric distances to the bow shock r_{BS} (red) and the magnetopause r_{MP} (black), and distance to the Wind spacecraft r_{Wind} (blue); (g) fluxes of electrons with energy $E_1 > 0.6$ MeV (black; legend on the left) and $E_2 > 2.0$ MeV (red; legend on the right); and (h) the geomagnetic SYM-H (black; legend on the left) and SML (red; legend on the right) indices. The MeV electron fluxes are given in the flux unit (fu), where an fu is electrons $\text{cm}^{-2} \text{s}^{-1} \text{sr}^{-1}$. The vertical dashed line indicates an interplanetary FF shock. The horizontal green bar shows an interplanetary sheath. A flux rope MC is indicated by a gray shading and a horizontal red bar on the top. The dark-blue shading inside the MC shows a sub-Alfvénic solar wind interval with $M_A < 1$.

consistent with results from previous related studies (e.g., Hajra & Tsurutani 2018b, pp. 373–400; Hajra et al. 2020).

At the trailing end of the sheath ($\sim 06:10$ UT on March 19), the IMF B_0 increases, and both N_{sw} and P_{sw} decrease sharply. As a consequence, V_A increases sharply (Figure 2(a), red), leading to an abrupt decrease in the M_A value (Figure 2(b)), and both the bow shock and magnetopause move sunward (Figure 2(f)). The IMF components exhibit a slow rotation up to $\sim 14:44$ UT on March 20 (Figure 2(e)). This represents a large-scale flux rope MC. The IMF B_z was mainly northward throughout the MC. The MC is associated with the slow recovery of the magnetic storm, as can be seen in the SYM-H variation (Figure 2(h), black). No substorms were triggered during the MC.

Inside the MC, N_{sw} drops below $\sim 1 \text{ cm}^{-3}$ at $\sim 02:27$ UT on March 20 (Figure 2(c), black), and V_A becomes comparable to or even larger than the solar wind V_{sw} ($\sim 350 \text{ km s}^{-1}$), and thus M_A becomes ≤ 1 . At the same time, a sharp sunward movement of the bow shock to beyond $\sim 80 R_\oplus$ is predicted from calculations. The bow shock crossed the Wind spacecraft location at $\sim 02:32$ UT on March 20 (Figure 2(f)).

At $\sim 10:37$ UT, N_{sw} exhibits another large drop to $\sim 0.21 \text{ cm}^{-3}$, and V_A attains a peak value of $\sim 627 \text{ km s}^{-1}$ (while V_{sw} was only $\sim 330 \text{ km s}^{-1}$). M_A remains significantly below 1 for ~ 4 hr, from $\sim 09:23$ to $\sim 13:23$ UT on March 20 (shown by the dark-blue shading in Figure 2). This event had a $\sim 98\%$ drop in plasma density compared to the background solar wind (outside the ICME interval). From the duration of the $M_A < 1$ interval and the solar wind speed, the radial extent of the sub-Alfvénic feature is estimated to be ~ 0.03 au along the Sun–Earth direction. To compare, the flux rope MC had an extent of ~ 0.29 au, ~ 1 order of magnitude higher than the sub-Alfvénic feature. The IMF B_0 varied between ~ 13 and ~ 21 nT (average

$B_0 \sim 14$ nT), the IMF angle with the Sun–Earth line ($\cos^{-1}(\mathbf{B} \cdot \hat{\mathbf{x}}/|\mathbf{B}|)$, $\hat{\mathbf{x}}$ is the unit vector directed from Earth to the Sun, and \mathbf{B} is the IMF vector) varied between 50° and 75° (average 62°) during the sub-Alfvénic interval. The plasma temperature T_{sw} varied between $\sim 0.4 \times 10^5$ K and $\sim 1.9 \times 10^5$ K. During the $M_A < 1$ interval, the bow shock disappeared, and the magnetopause moved to $\sim 18 R_\oplus$ from Earth.

During the sub-Alfvénic interval, there are no obvious impacts on the radiation belt MeV electron fluxes (Figure 2(g)), nor on the geomagnetic SYM-H and SML indices (Figure 2(h)). The peak SYM-H was only -24 nT, and it changed at a rate of $\sim 0.9 \text{ nT h}^{-1}$, indicating that no significant geomagnetic storm ring current enhancement was caused by the sub-Alfvénic wind. The SML peak was only -185 nT (at $\sim 13:25$ UT on March 20), indicating no obvious substorm triggering.

The IMF fluctuations on 2002 March 18–21 are examined by calculating the rms fluctuation levels and the nested variances, shown in Figure 3. The M_A variation and the interplanetary structure markings are repeated from Figure 2 for reference. Both the rms fluctuation levels (Figures 3(b)–(d)) and the normalized variances of the IMF components (Figures 3(e)–(g)) are found to increase with the arrival of the FF shock at $\sim 13:13$ UT on March 18 (shown by the vertical dashed line). They remain enhanced significantly during the sheath interval (green bar on the top). However, a clear reduction in the fluctuations can be noted during the MC (gray shaded region). Further reductions in the rms fluctuations and the variances are recorded from $\sim 02:27$ UT up to $\sim 13:23$ UT on March 20, when $M_A \leq 1$ (dark-blue shaded region). This result is consistent with Tsurutani et al. (1988) for MCs in general and with Smith et al. (2001) for a sub-Alfvénic interval in particular. While the large-scale (of the order of a few hours)

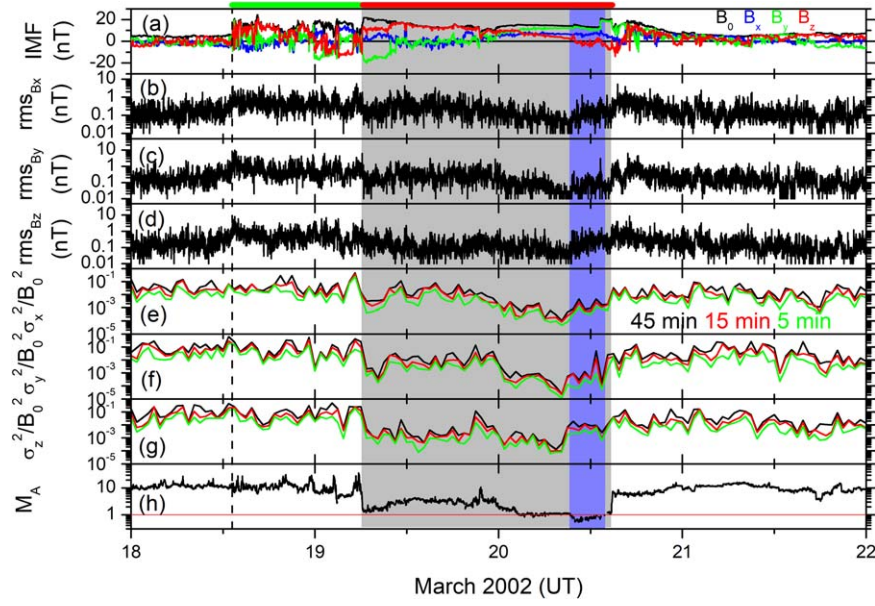


Figure 3. Variations of the IMF on 2002 March 18–21. From top to bottom, the panels are (a) the IMF B_0 (black) and B_x (blue), B_y (green), and B_z (red) components; (b–d) the rms variations in B_x , B_y , and B_z ; (e–g) the normalized variances in B_x , B_y , and B_z ; and (h) M_A . The markings for the interplanetary FF shock, sheath, and MC are the same as in Figure 2.

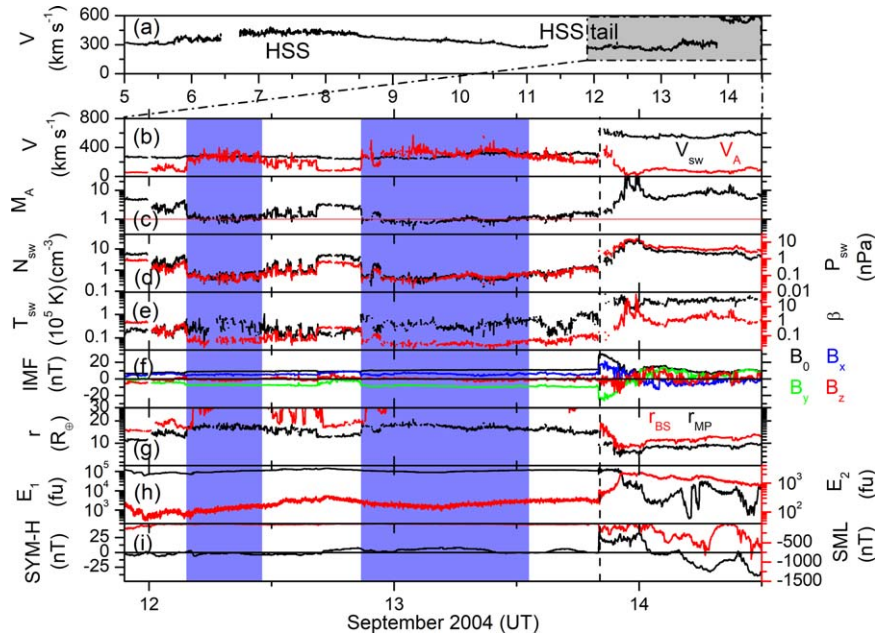


Figure 4. Solar wind measurements and geomagnetic effects on 2004 September 12–14. Panel (a) shows the V_{sw} variation from September 5 to 14. A weak HSS with peak V_{sw} of $\sim 478 \text{ km s}^{-1}$ on September 7 can be noted in the V_{sw} panel. The following panels (b)–(i) show the solar wind and geomagnetic variations during the HSS tail from September 12 to 14. Panels (b)–(i) starting from the second panel are in the same format as Figures 2(a)–(h), respectively.

IMF variations during the sub-Alfvénic wind are quite similar to the ambient variations of the MC, the magnetic fluctuations (of the order of a few minutes to less than an hour) are even more reduced during the sub-Alfvénic interval.

3.2. Sub-Alfvénic Solar Wind and Geomagnetic Variation on 2004 September 12–14

During 2004 September, the Wind spacecraft instrumentation made the solar wind measurements at $\sim 218 R_{\oplus}$ upstream of Earth (Figure 4). Wind encountered a weak HSS with a V_{sw} peak of $\sim 482 \text{ km s}^{-1}$ on September 7, as shown in Figure 4(a). The solar source is confirmed as a solar northern hemispheric

coronal hole in the SDO/AIA (171 Å) coronal image at $\sim 19:06 \text{ UT}$ on September 3 (not shown). It can be noted that the intrinsic coronal hole solar wind speeds are expected to range between ~ 750 and 800 km s^{-1} as shown by Ulysses observations (e.g., Phillips et al. 1994). Lower speeds (as in this case) are likely due to super-radial expansion in the interplanetary medium near the edges of the coronal hole (Tsurutani et al. 2011a). In the trailing part of the HSS, two sub-Alfvénic intervals are noted, from $\sim 03:36$ to $\sim 11:02 \text{ UT}$ on September 12 and from $\sim 20:53 \text{ UT}$ on September 12 to $\sim 13:12 \text{ UT}$ on September 13 (marked by dark-blue shadings in Figure 4).

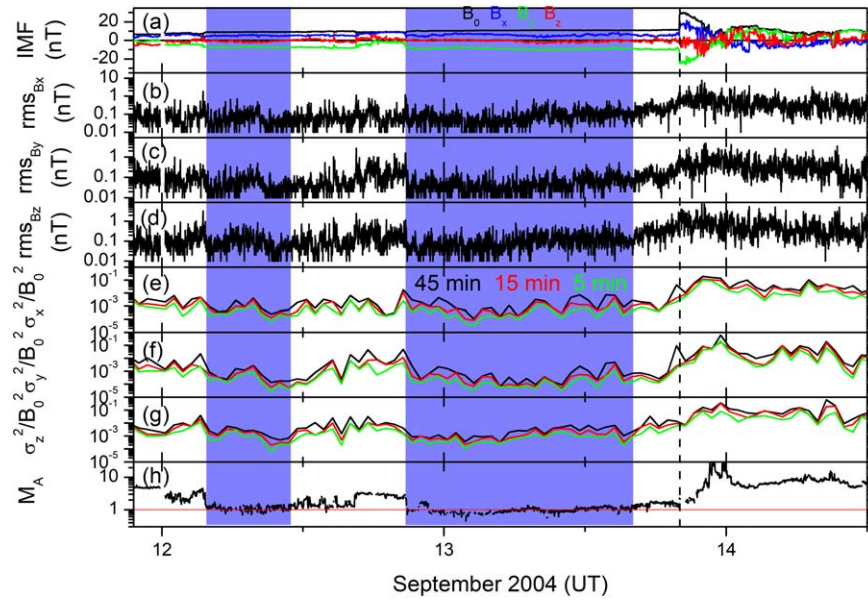


Figure 5. Variations of the interplanetary magnetic field on 2004 September 12–14. The panels are in the same format as in Figure 3.

During the sub-Alfvénic intervals, V_{sw} was reduced to $\sim 250\text{--}300\text{ km s}^{-1}$, $\sim 50\%$ of the HSS peak V_{sw} (Figure 4(b), black). The IMF components also exhibit monotonic variations without any large-scale variations in magnitude and direction (Figure 4(f)). The average IMF B_0 varied around ~ 9.1 and ~ 10.6 nT, with average angles of 53° and 52° relative to the Sun–Earth line during the two intervals, respectively. T_{sw} varied around 0.06×10^5 K to 0.59×10^5 K and 0.13×10^5 K to 0.53×10^5 K, respectively (Figure 4(e), black). However, the two sub-Alfvénic intervals are characterized by large drops in N_{sw} from the ambient values of $\sim 4.30\text{ cm}^{-3}$ (before the HSS arrival) to ~ 0.21 and $\sim 0.14\text{ cm}^{-3}$, respectively (Figure 4(d), black). These represent $\sim 95\%$ – 97% plasma density drops. As a consequence, the local Alfvén speed V_A increased up to $390\text{--}450\text{ km s}^{-1}$ (Figure 4(b), red). During the two intervals, the minimum values of M_A were ~ 0.70 and ~ 0.45 , respectively (Figure 4(c)). It can be concluded that these low M_A values resulted from the significantly reduced N_{sw} (while the solar wind speed V_{sw} is significantly lower than the peak HSS speed).

The sub-Alfvénic interval impacts cause a fast disappearance of the bow shock and the sunward movement of the magnetopause (Figure 4(g)). However, there are no significant impacts on the radiation belt MeV electron fluxes (Figure 4(h)), the ring current SYM-H index (Figure 4(i), black), or the auroral ionospheric SML index (Figure 4(i), red). During the two sub-Alfvénic intervals, the SYM-H index varied from $+3$ to -6 nT and from $+8$ to -2 nT, respectively, and the SML peaks were -28 and -18 nT, respectively.

A shock can be identified at $\sim 20:10$ UT on September 13 from the abrupt increases in V_{sw} , N_{sw} , P_{sw} , T_{sw} , and IMF B_0 . This is associated with the arrival of an ICME. However, since this occurs after the intervals of interest, this will not be discussed further. It can be surmised that the shock “contained” the HSS in its super-radial expansion. Otherwise, the expansion would have continued and even lower solar wind speeds would have been recorded.

Figure 5 shows the IMF fluctuations for the events of Figure 4. The IMF rms fluctuation levels are given in Figures 5(b)–(d), and the nested normalized variances are

given in Figures 5(e)–(g). Both sets of panels illustrate a reduction of the IMF fluctuations during the sub-Alfvénic intervals compared to the ambient variations. Interestingly, all three IMF components exhibit similar reductions in fluctuations.

3.3. Statistical Results

Among the 30 sub-Alfvénic solar wind intervals under study, 25 ($\sim 83\%$) occurred during MCs/driver gases identified with low β (as shown in Figure 2). Five ($\sim 17\%$) events occurred during passage of the trailing portions of HSSs (as shown in Figure 4). We estimated the minimum M_A , the average solar wind/interplanetary parameters N_{sw} , IMF B_0 , T_{sw} , V_{sw} , and V_A during each of the sub-Alfvénic winds. The results are summarized in Table 2 (for the MC-related events) and Table 3 (for the HSS-related events). For comparison, we also list the average values of the parameters for all available solar wind measurements referred to as the “average” solar winds in the tables. These are based on solar wind data (at 1 minute resolution) shifted to Earth’s bow shock nose for the period 1963–2020, obtained from the OMNIWeb (<http://omniweb.gsfc.nasa.gov/>). In order to study the impact of the sub-Alfvénic winds on the inner magnetosphere, we computed the rates of changes in the outer radiation belt MeV electron fluxes and the geomagnetic SYM-H and auroral ionospheric SML indices. We use rates of changes of the parameters for analyses that are more suitable indicators (than the absolute values) of any impacts caused by the sub-Alfvénic winds. The results are shown in Figure 6. As the IMF B_z southward component is the major factor controlling the inner magnetospheric impacts, distribution of average B_z during each sub-Alfvénic wind interval is also shown.

3.3.1. MC-related Events

For the MC-related events, the average sub-Alfvénic solar wind plasma speed V_{sw} was $\sim 532\text{ km s}^{-1}$, higher than the “average” solar wind V_{sw} of $\sim 434\text{ km s}^{-1}$ (Table 2). This is expected since all of these events were associated with fast ICMEs (average V_{sw} peak $\sim 729\text{ km s}^{-1}$ for all events). The

Table 2
Statistical Characteristics of the Sub-Alfvénic Solar Winds Related to MCs

Parameter	Minimum	Maximum	Mean \pm SD ^a	Median	“Average” Solar Wind
M_A	0.38	0.98	0.73 ± 0.16	0.75	9.7
V_A (km s ⁻¹)	410	1471	774 ± 302	685	48
Plasma β	0.003	0.037	0.011 ± 0.008	0.010	2.5
T_{sw} (10 ⁵ K)	0.08	12.46	2.00 ± 2.70	1.31	1.02
V_{sw} (km s ⁻¹)	328	949	532 ± 191	454	434
ICME peak V_{sw} (km s ⁻¹)	447	1135	729 ± 234	706	
N_{sw} (cm ⁻³)	0.04	1.19	0.41 ± 0.33	0.31	6.7
B_0 (nT)	8.3	53.9	21.9 ± 11.2	20.0	6.0
P_{sw} (nPa)	0.01	1.58	0.27 ± 0.33	0.18	2.3
r_{MP} (R_\oplus)	8.9	21.8	14.7 ± 3.0	13.8	11
r_{MP} increase (%)	33	86	56 ± 13	56	...

Note.

^a SD stands for the standard deviation from the mean.

Table 3
Statistical Characteristics of the Sub-Alfvénic Solar Winds Related to HSSs

Parameter	Minimum	Maximum	Mean \pm SD	Median	“Average” Solar Wind
M_A	0.45	0.84	0.68 ± 0.16	0.70	9.7
V_A (km s ⁻¹)	364	626	474 ± 115	417	48
Plasma β	0.008	0.020	0.014 ± 0.005	0.016	2.5
T_{sw} (10 ⁵ K)	0.06	0.46	0.31 ± 0.17	0.34	1.02
V_{sw} (km s ⁻¹)	234	388	304 ± 61	301	434
HSS peak V_{sw} (km s ⁻¹)	482	765	611 ± 126	643	
N_{sw} (cm ⁻³)	0.04	0.97	0.33 ± 0.37	0.21	6.7
B_0 (nT)	6.3	18.2	10.7 ± 4.5	9.4	6.0
P_{sw} (nPa)	0.01	0.18	0.06 ± 0.07	0.03	2.3
r_{MP} (R_\oplus)	14.8	21.0	18.0 ± 2.5	18.6	11
r_{MP} increase (%)	40	70	58 ± 13	59	...

Alfvén speed V_A of the sub-Alfvénic solar winds (~ 774 km s⁻¹) is significantly enhanced compared to the normal V_A of ~ 48 km s⁻¹. Thus, the low M_A values (of the sub-Alfvénic winds) resulted from the V_A enhancements and are not due to V_{sw} decreases. The V_A enhancements are attributed to the significant decreases in N_{sw} (~ 0.41 cm⁻³) compared to the average solar wind ($N_{sw} \sim 6.7$ cm⁻³). For these events, the IMF magnitude (average $B_0 \sim 22$ nT) was significantly larger than the normal solar wind average B_0 (~ 6 nT). The latter result is consistent with the events being within the MC high fields, a characteristic identified earlier.

In Figure 7, the location of the sub-Alfvénic region is shown relative to the spacecraft entering and exiting the MC. It is not known where in the MC the spacecraft entered and exited because only a single pass was made through the MC. However, the plot does give information as to where the sub-Alfvénic events were found. It is clear that the events are not only at the edges of the MC but throughout the MC.

During all of the MC-related sub-Alfvénic intervals, the bow shock nose disappeared promptly, and the calculated geocentric distance of the magnetopause increased by $\sim 33\%$ – 86% of the pre-event distance (Table 2). There were no significant changes in the outer radiation belt relativistic electron fluxes (changes were $<10\%$ h⁻¹ for the majority of the cases) (Figure 6(d)). No obvious substorms were triggered (Figure 6(c)), and the ring current activity was insignificant (Figure 6(b)), as can be observed from the SML and SYM-H changes, respectively. These results indicate no significant impacts of the sub-Alfvénic solar winds to the inner magnetosphere. However,

from the IMF B_z distribution (Figure 6(a)), few cases are found to have southward IMF components.

3.3.2. HSS-related Events

The five HSS-related sub-Alfvénic winds were noted to be located in the trailing portions of HSSs with average peak V_{sw} of ~ 611 km s⁻¹ for all events (Table 3). The sub-Alfvénic events are characterized by significantly lower N_{sw} (~ 0.33 cm⁻³), T_{sw} ($\sim 0.3 \times 10^5$ K), V_{sw} (~ 304 km s⁻¹), and V_A (~ 474 km s⁻¹) compared to those during average solar wind.

During the HSS-related sub-Alfvénic intervals, the bow shock nose exhibited fast evanescence and the calculated magnetopause distance from Earth became quite large (Table 3). However, the inner magnetosphere was more or less unaffected (Figure 6).

It should be noted that the solar wind velocities of the HSS sub-Alfvénic events are quite low. This is considerably different from those of the MC-related events. For the HSS-related events, all of the plasma parameters are substantially lower than those of the average solar wind, giving the exceptionally high V_A values.

4. Summary and Conclusions

The observations presented in this work have shown that the sub-Alfvénic intervals are found in two dynamical regions of the solar wind, in MCs/driver gases and in the trailing portions of HSSs. MCs/driver gases are one of three regions of CMEs

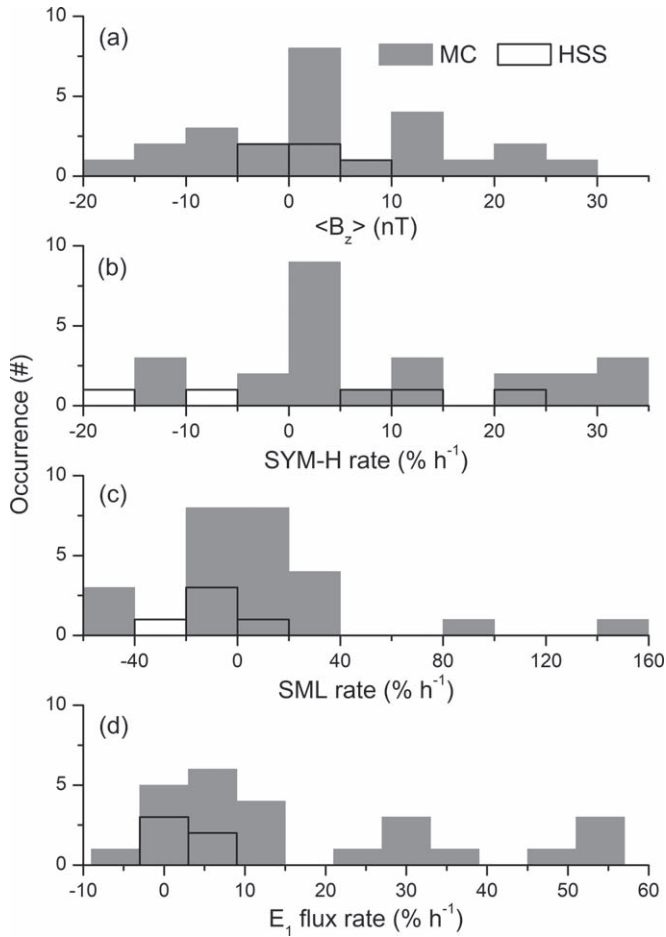


Figure 6. Histograms showing distributions of (a) IMF B_z , (b) SYM-H rate, (c) SML rate, and (d) $E_1 > 0.6$ MeV flux rate during (1) MC-related (gray filled histogram) and (2) HSS-related (open histogram) sub-Alfvénic winds.

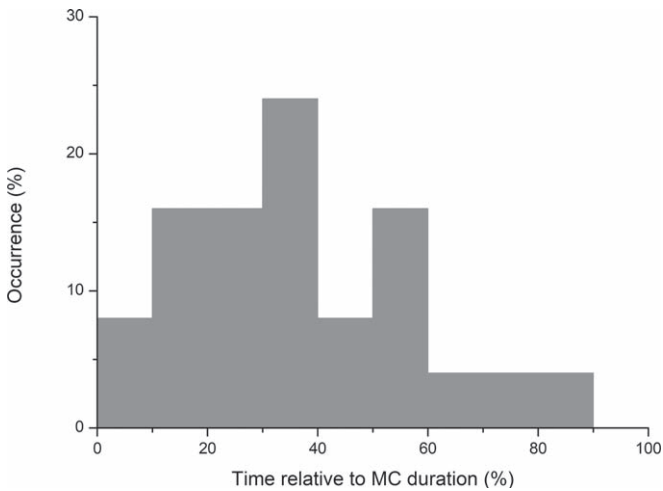


Figure 7. Distribution of the MC-related sub-Alfvénic event initiation relative to the MC duration. In the x-axis, 0% and 100% correspond to the MC start and end of the observation interval, respectively.

(observed at the Sun) and typically the only part of a CME observed at 1 au.

The MC-related sub-Alfvénic events are characterized by high IMF B_0 and low T_{sw} and therefore low β . This has been found to be characteristic of fast MCs/driver gases (Burlaga et al. 1981; Tsurutani et al. 1988), as well as slow MCs

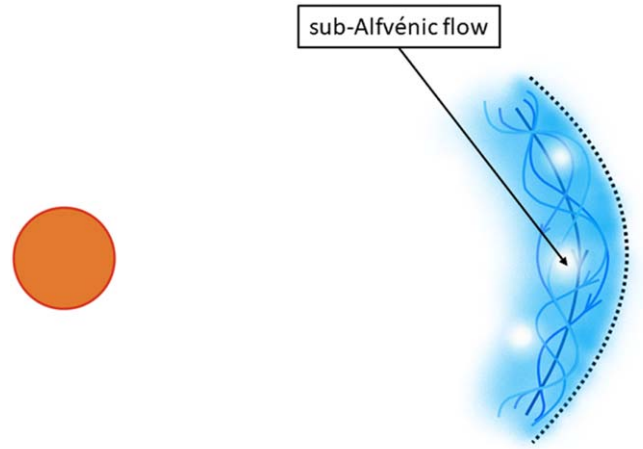


Figure 8. A schematic of a flux rope MC extending from the Sun to beyond 1 au. Blue lines show magnetic field lines associated with the magnetic flux rope. The plasma density is indicated by coloring, dark blue being the highest, then light blue, and then white.

(Tsurutani et al. 2004). The only parameter that sets things apart for the sub-Alfvénic solar wind intervals are the exceptionally low N_{sw} values. The sub-Alfvénic intervals, characterized by extremely low plasma density, can be viewed as being caused by evolution of the MCs in interplanetary space. Why have the sub-Alfvénic intervals been related to only fast MCs/driver gases? One possibility is that faster ICME events expand more both in heliolatitude and in heliolongitude and therefore take up considerably more volume as they propagate away from the Sun. This will lead to significant small pockets of low plasma densities. Our supposition is shown in the schematic in Figure 8. It should be noted that while the schematic shows a flux rope magnetic field configuration, many different types of magnetic field were noted from the events in this study. We attempted to find some unifying picture of the non-flux rope events but were unable to do so.

The schematic in Figure 8 shows the sub-Alfvénic solar wind intervals randomly located within the magnetic flux rope/driver gas region. This is consistent with the findings of Figure 7.

In the case of the sub-Alfvénic events occurring in the trailing portion of HSSs, the velocities of the sub-Alfvénic events were a fraction ($\sim 50\%$) of the peak HSS speeds. It was also noted that the events had low N_{sw} , low T_{sw} , and average IMF B_0 values, consistent with plasma properties expected in the trailing portion of HSSs. A rarefaction region with decreased plasma densities, decreased temperatures, and average magnetic fields is created in the trailing portion of an HSS (Sarabhai 1963; Parker 1965; Tsurutani et al. 2011a). The latter region is where the sub-Alfvénic plasma regions are located. A schematic of this is shown in Figure 9.

Our hypothesis is that both types of these sub-Alfvénic events are created by evolution within the interplanetary medium, not by features intrinsic to the Sun or to solar phenomena.

What will happen as these solar wind features propagate further into the distant heliosphere? For the MC-related events, it can be expected that further spatial expansion of the MCs will cause enlargement of the sub-Alfvénic regions and that they will cause the disappearance of the bow shocks of Jupiter

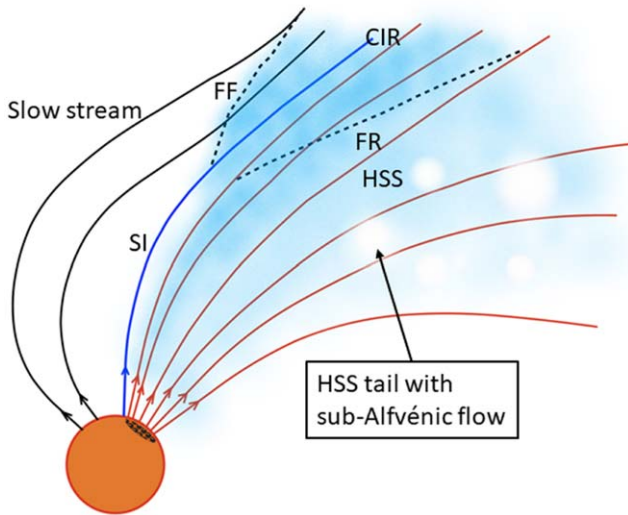


Figure 9. A schematic of the solar wind HSS from the Sun to beyond 1 au, viewed from the Sun's north pole. The coronal hole is indicated by a dark region on the Sun. Magnetic field lines emanating from the coronal hole are shown in red. The slow solar wind magnetic field lines are shown in black. The compressed plasma and magnetic field region of the CIR is bounded by fast forward (FF) and fast reverse (FR) shocks at sunward and antisunward locations. The CIR is indicated by blue shading, and the shocks are shown by dashed lines. The HSS and slow solar wind are separated by a stream interface (SI) shown by a blue line. To the right of magnetic field lines that intersect the CIR is the trailing part of the HSS. The location of the sub-Alfvénic plasma cavities created by super-radial expansion is indicated.

(at ~ 5 au) and Saturn (at ~ 10 au) with consequential temporary expansions of their magnetospheres.

What about the HSS-related sub-Alfvénic events? Super-radial expansion may occur in only a limited region of the heliosphere, somewhat close to the Sun and Earth. Thus, such HSS-related sub-Alfvénic solar winds may not be present at much greater radial distances. Thus, we expect that the disappearance of bow shocks at Jupiter and Saturn may be due to only MC-related sub-Alfvénic events. In fact, if our model/supposition is correct, there may be more of these sub-Alfvénic intervals upstream of Jupiter and Saturn.

Another significant finding of this work is reduced magnetic field fluctuations as evidenced from low magnetic field variances in the sub-Alfvénic intervals. A lack of Alfvén waves in these intervals was previously noted by Smith et al. (2001). What do the low magnetic field variances mean in physical terms? During the sub-Alfvénic intervals, the plasma moves slower than the Alfvén wave group velocity ($V_{sw} < V_A$). Thus, the slower plasma can be accelerated by the wave electric field to move closer to the wave group velocity and gain energy from the wave. This may lead to a net damping of the waves, or “Landau damping” (Landau 1946; Tsurutani & Smith 1974; Tsurutani & Lakhina 1997).

The work of R.H. is funded by the Science and Engineering Research Board (SERB), a statutory body of the Department of Science and Technology (DST), Government of India through the Ramanujan Fellowship. Portions of this effort were performed at the Jet Propulsion Laboratory, California Institute of Technology under contract with NASA. B.T.T. thanks ISSI in Bern Switzerland for support of the International Team #455 on “Complex Systems Perspectives Pertaining to the Research of the Near-Earth Electromagnetic Environment” under which this paper was written. The solar wind plasma and

magnetic field measurements are taken from the IMP 8 (https://spdf.gsfc.nasa.gov/pub/data/imp/imp8/mag/15s_ascii_v3/), Geotail (<https://cdaweb.gsfc.nasa.gov/cgi-bin/eval1.cgi>), ACE (<http://www.srl.caltech.edu/ACE/ASC/>), and Wind (<https://spdf.gsfc.nasa.gov/pub/data/wind/>) spacecraft. The solar wind data shifted to Earth's bow shock nose are obtained from the OMNIWeb (<http://omniweb.gsfc.nasa.gov/>). The sunspot numbers are obtained from the Royal Observatory of Belgium, Brussels (<http://www.sidc.be/silso/home>). The CME information is obtained from the CDAW SOHO/LASCO CME catalog (<https://cdaw.gsfc.nasa.gov/CMElist/index.html>). The SDO/AIA solar coronal images are obtained from <https://sdo.gsfc.nasa.gov/>, and the SWPC solar synoptic maps are obtained from <https://www.swpc.noaa.gov/products/solar-synoptic-map>. The geomagnetic SYM-H indices are taken from the World Data Center for Geomagnetism, Kyoto, Japan (<http://wdc.kugi.kyoto-u.ac.jp/>). The auroral ionospheric SML indices are obtained from SuperMAG (<https://supermag.jhuapl.edu/>). The geosynchronous orbit MeV electron fluxes are obtained from <http://www.ngdc.noaa.gov/stp/satellite/goes/dataaccess.html>. We would like to thank the reviewer for extremely valuable suggestions that substantially improved the manuscript.

ORCID iDs

Rajkumar Hajra  <https://orcid.org/0000-0003-0447-1531>

References

- Abraham-Shrauner, B., & Yun, S. H. 1976, *JGR*, **81**, 2097
- Akasofu, S.-I. 1964, *P&SS*, **12**, 273
- Burlaga, L., Sittler, E., Mariani, F., & Schwenn, R. 1981, *JGRA*, **86**, 6673
- Chané, E., Raeder, J., Saur, J., et al. 2015, *JGRA*, **120**, 8517
- Chané, E., Saur, J., Neubauer, F. M., Raeder, J., & Poedts, S. 2012, *JGRA*, **117**, A09217
- Chapman, S., & Bartels, J. 1940, *Geomagnetism*, Vol. 1 (Oxford: Oxford Univ. Press)
- Chapman, S., & Ferraro, V. C. A. 1931, *TeMAE*, **36**, 77
- Clarke, J. T., Ajello, J., Ballester, G., et al. 2002, *Natur*, **415**, 997
- Cohen, O., Drake, J. J., Gloer, A., et al. 2014, *ApJ*, **790**, 57
- Dessler, A. J., & Parker, E. N. 1959, *JGRA*, **64**, 2239
- Fairfield, D. H. 1971, *JGRA*, **76**, 6700
- Fairfield, D. H., Iver, H. C., Desch, M. D., et al. 2001, *JGRA*, **106**, 25361
- Farris, M. H., & Russell, C. T. 1994, *JGRA*, **99**, 17681
- Gjerloev, J. W. 2009, *Eos Trans. AGU*, **90**, 230
- Gonzalez, W. D., Joselyn, J. A., Kamide, Y., et al. 1994, *JGRA*, **99**, 5771
- Gosling, J. T., Asbridge, J. R., Bame, S. J., et al. 1982, *JGRA*, **87**, 239
- Grodent, D., Gérard, J.-C., Gustin, J., et al. 2006, *GeoRL*, **33**, L06201
- Hajra, R. 2021, *ApJ*, **917**, 91
- Hajra, R., Echer, E., Tsurutani, B. T., & Gonzalez, W. D. 2013, *JGRA*, **118**, 5626
- Hajra, R., Henri, P., Vallières, X., et al. 2017, *A&A*, **607**, A34
- Hajra, R., & Tsurutani, B. T. 2018a, *ApJ*, **858**, 123
- Hajra, R., & Tsurutani, B. T. 2018b, in *Extreme Events in Geospace: Origins, Predictability, and Consequences*, ed. N. Buzulukova (Amsterdam: Elsevier)
- Hajra, R., Tsurutani, B. T., Echer, E., Gonzalez, W. D., & Gjerloev, J. W. 2016, *JGRA*, **121**, 7805
- Hajra, R., Tsurutani, B. T., & Lakhina, G. S. 2020, *ApJ*, **899**, 3
- Hugoniot, H. 1887, *Journal de l'École Polytechnique*, **57**, 3
- Hugoniot, H. 1889, *Journal de l'École Polytechnique*, **58**, 1
- Illing, R. M. E., & Hundhausen, A. J. 1986, *JGR*, **91**, A10
- Iyemori, T., Takeda, M., Nose, M., Odagi, Y., & Toh, H. 2010, *Mid-latitude Geomagnetic Indices ASY and SYM for 2009 (Provisional)*, Internal Report of Data Analysis Center for Geomagnetism and Space Magnetism, Kyoto University, <http://wdc.kugi.kyoto-u.ac.jp/aeasy/asy.pdf>
- Kennel, C. F., Edmiston, J. P., & Hada, T. 1985, in *Collisionless Shocks in the Heliosphere: A Tutorial Review*, ed. R. G. Stone & B. T. Tsurutani (Washington, D.C: AGU)
- Kivelson, M., Khurana, K., Joy, S., et al. 1997, *Sci*, **276**, 1239

- Klein, L. W., & Burlaga, L. F. 1982, *JGRA*, **87**, 613
- Kriegel, H., Simon, S., Motschmann, U., et al. 2011, *JGRA*, **116**, A10223
- Krieger, A. S., Timothy, A. F., & Roelof, E. C. 1973, *SoPh*, **29**, 505
- Landau, L. P. 1946, *JPh*, **10**, 25
- Lemen, J. R., Title, A. M., Akin, D. J., et al. 2012, *SoPh*, **275**, 17
- Lepping, R. P., Acuña, M. H., Burlaga, L. F., et al. 1995, *SSRv*, **71**, 207
- Lugaz, N., Farrugia, C., Huang, C. L., et al. 2016, *NatCo*, **7**, 13001
- McIlwain, C. E. 1961, *JGRA*, **66**, 3681
- Mura, A., Adriani, A., Connerney, J. E. P., et al. 2018, *Sci*, **361**, 774
- Ogilvie, K. W., Chornay, D. J., Fritzenreiter, R. J., et al. 1995, *SSRv*, **71**, 55
- Onsager, T., Grubb, R., Kunches, J., et al. 1996, *Proc. SPIE*, **2812**, 281
- Parker, E. N. 1965, *SSRv*, **4**, 666
- Pesnell, W. D., Thompson, B. J., & Chamberlin, P. C. 2012, *SoPh*, **275**, 3
- Phillips, J. L., Balogh, A., Bame, S. J., et al. 1994, *GeoRL*, **21**, 1105
- Rankine, W. J. M. 1870, *RSPT*, **160**, 277
- Sarabhai, V. 1963, *JGRA*, **68**, 1555
- Saur, J., Grambusch, T., Duling, S., Neubauer, F. M., & Simon, S. 2013, *A&A*, **552**, A119
- Sheeley, N. R., Harvey, J. W., & Feldman, W. C. 1976, *SoPh*, **49**, 271
- Shkolnik, E., Walker, G. A. H., Bohlender, D. A., Gu, P.-G., & Kürster, M. 2005, *ApJ*, **622**, 1075
- Shue, J.-H., Song, P., Russell, C. T., et al. 1998, *JGRA*, **103**, 17691
- Smith, C. W., Mullan, D. J., Ness, N. F., Skoug, R. M., & Steinberg, J. 2001, *JGRA*, **106**, 18625
- Smith, E. J. 1985, in *Collisionless Shocks in the Heliosphere: Reviews of Current Research*, ed. B. T. Tsurutani & R. G. Stone (Washington, DC: AGU)
- Smith, E. J., & Wolfe, J. H. 1976, *GeoRL*, **3**, 137
- Tsurutani, B. T., Echer, E., & Gonzalez, W. D. 2011a, *AnGeo*, **29**, 839
- Tsurutani, B. T., Echer, E., Guarnieri, F. L., & Gonzalez, W. D. 2011b, *JASTP*, **73**, 164
- Tsurutani, B. T., Gonzalez, W. D., Gonzalez, A. L. C., et al. 1995, *JGR*, **100**, 21717
- Tsurutani, B. T., Gonzalez, W. D., Tang, F., Akasofu, S. I., & Smith, E. J. 1988, *JGRA*, **93**, 8519
- Tsurutani, B. T., & Gonzalez, W. D. 1997, in *Magnetic Storms*, ed. B. T. Tsurutani (Washington, DC: AGU)
- Tsurutani, B. T., Gonzalez, W. D., Zhou, X. Y., Lepping, R. P., & Bothmer, V. 2004, *JASTP*, **66**, 147
- Tsurutani, B. T., Hajra, R., Tanimori, T., et al. 2016, *JGRA*, **121**, 10130
- Tsurutani, B. T., Jones, D. E., Slavin, J. A., Sibeck, D. G., & Smith, E. J. 1984, *GeoRL*, **11**, 1062
- Tsurutani, B. T., & Lakhina, G. S. 1997, *RvGeo*, **35**, 491
- Tsurutani, B. T., Lakhina, G. S., Echer, E., et al. 2018, *JGRA*, **123**, 1388
- Tsurutani, B. T., Lakhina, G. S., Verkhoglyadova, O. P., et al. 2011c, *JASTP*, **73**, 5
- Tsurutani, B. T., & Lin, R. P. 1985, *JGRA*, **90**, A1
- Tsurutani, B. T., & Smith, E. J. 1974, *JGRA*, **79**, 118
- Tsurutani, B. T., Smith, E. J., Pyle, K. R., & Simpson, J. A. 1982, *JGRA*, **87**, 7389
- Usmanov, A. V., Goldstein, M. L., & Farrell, W. M. 2000, *GeoRL*, **27**, 3765
- Usmanov, A. V., Goldstein, M. L., Ogilvie, K. W., Farrell, W. M., & Lawrence, G. R. 2005, *JGRA*, **110**, A01106
- Wanliss, J. A., & Showalter, K. M. 2006, *JGRA*, **111**, A02202
- West, H., Buck, R., & Walton, J. 1972, *NPhS*, **240**, 6
- Zhou, X., Tsurutani, B. T., & Gonzalez, W. D. 2000, *GeoRL*, **27**, 4025